

Spatiotemporal chaos in the dynamics of buoyantly and diffusively unstable chemical fronts

M. P. M. A. Baroni, E. Guéron, and A. De Wit

Citation: *Chaos* **22**, 013134 (2012); doi: 10.1063/1.3695339

View online: <http://dx.doi.org/10.1063/1.3695339>

View Table of Contents: <http://chaos.aip.org/resource/1/CHAOEH/v22/i1>

Published by the [American Institute of Physics](#).

Related Articles

Instability of a transverse liquid rivulet on an inclined plane

Phys. Fluids **24**, 032104 (2012)

A snapshot of electrified nanodroplets undergoing Coulomb fission

Appl. Phys. Lett. **100**, 074103 (2012)

Inertial-range anisotropy in Rayleigh-Taylor turbulence

Phys. Fluids **24**, 025101 (2012)

Nonlinear effects in the combined Rayleigh-Taylor/Kelvin-Helmholtz instability

Phys. Fluids **23**, 114107 (2011)

Experimental observation of standing interfacial waves induced by surface waves in muddy water

Phys. Fluids **23**, 096603 (2011)

Additional information on Chaos

Journal Homepage: <http://chaos.aip.org/>

Journal Information: http://chaos.aip.org/about/about_the_journal

Top downloads: http://chaos.aip.org/features/most_downloaded

Information for Authors: <http://chaos.aip.org/authors>

ADVERTISEMENT



AIP Advances

Submit Now

**Explore AIP's new
open-access journal**

- **Article-level metrics
now available**
- **Join the conversation!
Rate & comment on articles**

Spatiotemporal chaos in the dynamics of buoyantly and diffusively unstable chemical fronts

M. P. M. A. Baroni,^{1,a)} E. Guéron,^{1,b)} and A. De Wit^{2,c)}

¹*Centro de Matemática, Computação e Cognição, Universidade Federal do ABC, 09210-170 Santo André-SP, Brazil*

²*Nonlinear Physical Chemistry Unit and Service de Chimie Physique et Biologie Théorique, Faculté des Sciences, Université Libre de Bruxelles (ULB), CP 231, 1050 Brussels, Belgium*

(Received 3 October 2011; accepted 28 February 2012; published online 23 March 2012)

Nonlinear dynamics resulting from the interplay between diffusive and buoyancy-driven Rayleigh-Taylor (RT) instabilities of autocatalytic traveling fronts are analyzed numerically for various values of the relevant parameters. These are the Rayleigh numbers of the reactant A and autocatalytic product B solutions as well as the ratio $D = D_B/D_A$ between the diffusion coefficients of the two key chemical species. The interplay between the coarsening dynamics characteristic of the RT instability and the constant short wavelength modulation of the diffusive instability can lead in some regimes to complex dynamics dominated by irregular succession of birth and death of fingers. By using spectral entropy measurements, we characterize the transition between order and spatial disorder in this system. The analysis of the power spectrum and autocorrelation function, moreover, identifies similarities between the various spatial patterns. The contribution of the diffusive instability to the complex dynamics is discussed. © 2012 American Institute of Physics. [<http://dx.doi.org/10.1063/1.3695339>]

Interaction between two different instabilities is known to yield spatiotemporal chaos (STC) in some cases. We analyze here such STC when diffusive and buoyancy-driven Rayleigh-Taylor instabilities of autocatalytic fronts interact. The diffusive instability arises when reactants A ahead of the front have a diffusion coefficient D_A much larger than the diffusion coefficient D_B of the products behind it. It leads to cm-long periodic modulations of the front developing after a few hours and the dynamics of which becomes irregular in time and space for sufficiently small values of the ratio $D = D_B/D_A$. A convective RT instability arises on the other hand when the reactants and products have different densities such that the denser part of the front lies above the less dense one in the gravity field. Periodic flow vortices of the order of a few millimeters deform then the front within a few minutes. Interaction between these two instabilities can lead to complex dynamics including spatiotemporal chaos. On the basis of numerical simulations of the problem, we apply quantitative characterization of the STC obtained when these diffusive and RT instabilities of autocatalytic fronts interact. This gives insight into the respective contribution of diffusive and convective modes to the observed STC.

I. INTRODUCTION

Complex spatiotemporal dynamics are known to occur when, for instance, two instabilities characterized by different

characteristic length and time scales interact.¹ Recently, a new example of such complexity arising from interplay between two different instabilities has been evidenced in the dynamics of autocatalytic fronts subject to both diffusive and convective instabilities.²⁻⁵

Chemical fronts whereby autocatalytic products invade fresh reactants at constant speed can indeed become unstable because of two different kinds of instabilities. The first one is due to differential diffusion effects. The corresponding diffusive instability appears when the reactants diffuse sufficiently faster than the products, in effect when the ratio $D = D_B/D_A$ between the diffusion coefficients of the product B and the reactant A is smaller than a critical value D_c , the value of which depends on the kinetics of the reaction. A spatial modulation of the front with a wavelength of the order of cm appears on a time scale of a few hours.⁶⁻¹² As an example, this diffusive instability has been studied theoretically for the cubic autocatalytic reaction



where c_a and c_b are, respectively, the concentrations of reactant A and autocatalyst B , and k_0 is a kinetic constant. For this reaction, the critical diffusion ratio below which the planar front loses diffusively its stability under transverse perturbations is $D_c = 0.43$. One single length scale characterizes the front modulation for $D \leq D_c$, while two characteristic lengths interact for smaller D leading to spatio-temporal chaos.⁷

Fronts can also become unstable because of unfavorable density gradients across the front. In absence of gels, these gradients can trigger convective flows due to buoyancy effects in the gravity field.¹³⁻¹⁷ Typically, a Rayleigh-Taylor (RT) instability can appear when a denser solution lies on

^{a)}Electronic mail: mariana.baroni@gmail.com.

^{b)}Electronic mail: eduardo.gueron@ufabc.edu.br.

^{c)}Electronic mail: adewit@ulb.ac.be.

top of a less dense one in the gravity field, which is possible as soon as the reactant A has a different density than the product B. For some reactions¹⁵ like typically the iodate-arsenous acid reaction, reactants are denser than the products and ascending fronts are buoyantly unstable¹⁶ while for other reactions such as the chlorite-tetrathionate one, for example, the opposite is true: products are denser than reactants and descending fronts are those that are unstable.¹⁷

Recent theoretical²⁻⁴ work have shown that, when these two instabilities interact, complex spatiotemporal dynamics in the form of irregular succession of birth and death of fingers can be obtained. D'Hernoncourt *et al.*⁴ have characterized numerically these nonlinear dynamics in terms of mixing length, averaged concentration profiles and, especially, space-time maps. Such maps which show the evolution in time of the location of minima and maxima of fingers clearly demonstrate that spatiotemporal chaos (STC) is obtained when diffusive and RT instabilities of fronts interact. From the experimental point of view, it is challenging to obtain interaction between diffusive and convective instabilities as they both usually operate on very different time scales. A first step in that direction has been achieved by Rica *et al.* who have experimentally shown that buoyancy-driven dynamics around autocatalytic fronts can be influenced by a difference in the diffusion coefficient of the reactant and autocatalytic product.⁵ Further developments need, however, to be done from an experimental point of view to further study the coupling between diffusive and convective instabilities.

In this context, it is of interest to further quantify theoretically the properties of the expected complex STC dynamics in order to understand the relative weight of the diffusive and convective modes in the degree of complexity of the spatiotemporal evolution of the variables. In particular, as it is known that STC is already obtained for diffusively unstable systems without convective effects when D is sufficiently smaller than D_c , we want to understand to what extent the properties of STC differ when only one or both instabilities come into play. To do so, we numerically integrate, using the cubic kinetics (1), a reaction-diffusion-convection model which can feature both diffusive and RT instabilities. We first focus on the pure reaction-diffusion system and analyze the properties of diffusively unstable fronts and of the related STC as a function of the parameter D . We next couple this instability to the convective RT one and analyze the changes in properties of diffusive STC when convection comes into play.

The present article is, therefore, organized as follows. In Sec. II, we present the model which describes the interplay between diffusive and RT instabilities. Section III introduces quantitative methods to identify and characterize transitions from regular patterns to complex spatio-temporal dynamics. Results are discussed in Sec. IV and conclusions presented in Sec. V.

II. MODEL AND NUMERICAL SCHEME

We consider the autocatalytic reaction $A + 2B \rightarrow 3B$ within a two-dimensional porous medium or Hele-Shaw cell

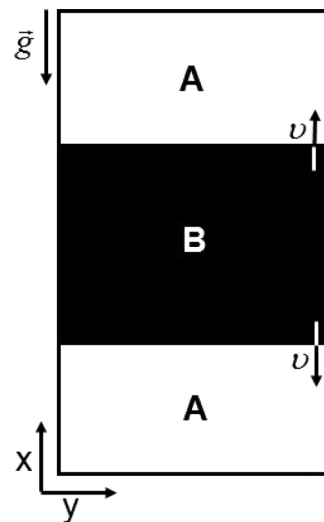


FIG. 1. Sketch of the system.

of length L_x and width L_y , vertically oriented (see Fig. 1). When coupled to diffusion, this reaction is known to provide traveling fronts. We start from a system filled with the reactant A and a band of product B in the middle such that it leads to both downward and upward propagating fronts. When unfavorable density gradients develop around the front, convective motions can appear. The concentrations c_a and c_b of reactant A and autocatalytic product B follow then reaction-diffusion-convection dynamics described by the following equations:²⁻⁴

$$\nabla \cdot \mathbf{u} = 0, \quad (2)$$

$$\nabla p = -\frac{\mu}{\kappa} \mathbf{u} - \rho(a, b) \mathbf{g} \mathbf{e}_x, \quad (3)$$

$$\frac{\partial c_a}{\partial t} + \mathbf{u} \cdot \nabla c_a = D_A \nabla^2 a - k_0 c_a c_b^2, \quad (4)$$

$$\frac{\partial c_b}{\partial t} + \mathbf{u} \cdot \nabla c_b = D_B \nabla^2 b + k_0 c_a c_b^2. \quad (5)$$

Here, the velocity field $\mathbf{u} = (u_x, u_y)$ of the incompressible flow is described by two-dimensional Darcy's law (Eqs. (2) and (3)) written in the Boussinesq approximation. p represents the pressure and κ is the permeability of the porous medium. $k_0 c_a c_b^2$ is the reaction rate where k_0 is the kinetic constant. The diffusion coefficients $D_{A,B}$ of A and B, the gravitational acceleration g and the viscosity μ are all assumed constant.

The density is given by an equation of state $\rho(a, b) = \rho_0 + \gamma_a c_a + \gamma_b c_b$ where $\rho_0 = \rho(0, 0)$ is the fluid density of the solvent and $\gamma_{a,b}$ are the positive solutal expansion coefficients of species A and B, respectively.²⁻⁴

Let us then introduce the time scale $T_0 = \frac{1}{k_0 c_{a0}^2}$, the length scale $L_0 = \sqrt{D_A T_0}$, and the characteristic velocity $U_0 = \sqrt{D_A / T_0}$. The density scales with $\delta\rho = (\gamma_a - \gamma_b) c_{a0}$, i.e., the density jump across the front. The dimensionless equations are then²⁻⁴

$$\nabla \cdot \mathbf{u} = 0, \quad (6)$$

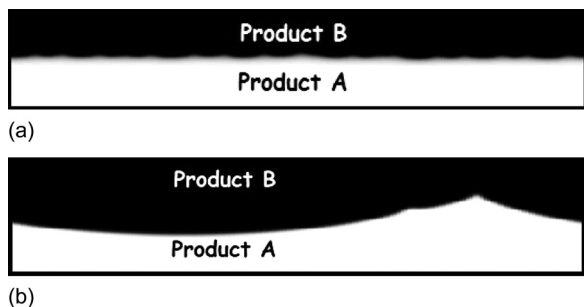


FIG. 2. Example of interface modulation for a descending front due to (a) diffusive instability $R_a = R_b = 0, D = 0.15$ and (b) a Rayleigh-Taylor instability for $R_b > R_a, D = 0.6$. Size of the image: 86×256 .

$$\nabla p = -u + [R_a c_a + R_b c_b] \hat{z}, \tag{7}$$

$$\frac{\partial c_a}{\partial t} + u \cdot \nabla c_a = \nabla^2 c_a - c_a c_b^2, \tag{8}$$

$$\frac{\partial c_b}{\partial t} + u \cdot \nabla c_b = D \nabla^2 c_b + c_a c_b^2, \tag{9}$$

where the diffusion coefficients ratio D and the Rayleigh numbers R_a and R_b are given by

$$D = \frac{D_B}{D_A}, \quad R_a = \frac{\gamma_a \kappa g}{\mu \sqrt{D_A k_0}}, \quad R_b = \frac{\gamma_b \kappa g}{\mu \sqrt{D_B k_0}}. \tag{10}$$

In absence of flow, i.e., when $R_a = R_b = 0$, the reaction-diffusion system (8) and (9) with $u = 0$ can feature a diffusive instability provided the system is large enough and $D < D_c$, where $D_c = 0.43$ for the cubic scheme chosen here.^{2,6,7,12} Such a diffusive instability is independent of



FIG. 3. Example of a dynamics where RT and diffusive instabilities interact for $R_b > R_a, D = 0.1$. Size of the image: 121×256 .

gravity and affects thus both upward and downward traveling fronts (see Fig. 2(a)). In spatially extended systems, spatio-temporal chaos is then observed.^{6,7} If $D > D_c$, the front is diffusionally stable. For any value of D , the front can also become buoyantly unstable if density gradients operate across the front. If the density decreases during the reaction (reactants denser than products, i.e., $R_a > R_b$), the ascending fronts are buoyantly unstable while, for increasing density ($R_a < R_b$), the descending fronts are buoyantly unstable^{3,4} (Fig. 2(b)). If $D < D_c$ and $R_a \neq R_b$, then both instabilities can operate simultaneously.

To analyze the relevant dynamics numerically, the dimensionless equations (6)–(9) are solved using a pseudo-spectral numerical method introduced by Tan and Homsy¹⁸ and adapted to take the chemical reaction into account. The boundary conditions are periodic in x and y directions, while the initial conditions are $c_a = 1, c_b = 0$ and no flow. A local horizontal noise input of B in the middle of the system initiates the traveling front (see Fig. 1). Each simulation starts with exactly the same noise in a system of dimensionless length $L_x = 8192$ and width $L_y = 512$. The spatial discretization uses a ratio of 2 between the number of spectral modes N_y and N_x and the dimensionless width L_y and length L_x . Hence, the

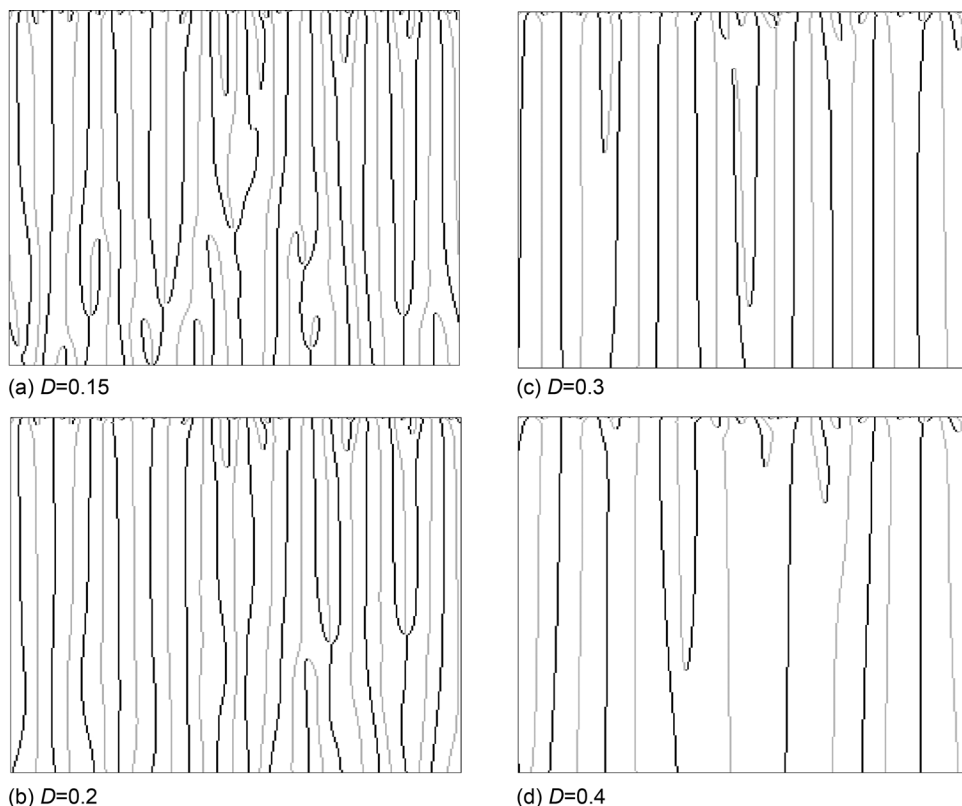


FIG. 4. Space-time map of the locations of the maxima (black) and minima (grey) of the longitudinally averaged profile of c_a as a function of time (increasing downwards from $t=0$ to $t=5000$) for the pure diffusive instability and various values of D . $R_{a,b} = 0$.

computational domain has here $N_x = 4096$ and $N_y = 256$ nodes. The time step is $dt = 0.2$. The ratio $\alpha = \frac{R_b}{R_a} = \frac{\gamma_b}{\gamma_a}$ is here kept constant. We study three different cases $R_b = \alpha R_a$: $\alpha = 0$, $\alpha = 0.5$, and $\alpha = 2$ for various values of D . Our objective is to characterize spatio-temporal complexity arising when the RT and diffusive instabilities interact. Before doing so, let us introduce the various tools used to quantify spatio-temporal complexity. These tools will first be used to characterize the pure diffusive instability before convection will be added to the problem.

III. QUANTITATIVE AND QUALITATIVE MEASURES

Nonlinear dynamics can be analyzed by studying the evolution of the two-dimensional (2D) concentration fields $c_{a,b}(x, y, t)$ such as shown in Figs. 2 and 3 in the course of time. At successive times, these 2D concentration fields can be spatially averaged along the longitudinal x coordinate in half the system where the front propagates to yield one-dimensional (1D) averaged profiles defined by¹⁹:

$$\langle c_{a,b}(y, t) \rangle = \frac{2}{L_x} \int_0^{L_x/2} c_{a,b}(x, y, t) dx. \quad (11)$$

For a stable front, the front is flat and hence $\langle c_{a,b}(y, t) \rangle$ remains constant and equal to the mean concentration in the cell. For unstable systems, this measure allows one to follow the number of fingers in time and, in particular, shows how the fingers interact: some fingers can spread and shield their neighbors, while others merge to ultimately lead, in some cases, to one asymptotic single finger.^{19,20}

These longitudinally averaged profiles also enable to distinguish different characteristics of finger patterns when they are used to plot space-time maps. These maps show the location of the maxima and minima of the longitudinally averaged profile $\langle c_{a,b}(y, t) \rangle$ in the course of time.^{4,20} The resulting system's dynamics for diffusively unstable fronts is presented in Figure 4 for $R_a = R_b = 0$ and different values of D below D_c .

In these spatio-temporal maps, one can see that, for $D = 0.4$, the wavelength of fingers remains almost constant.

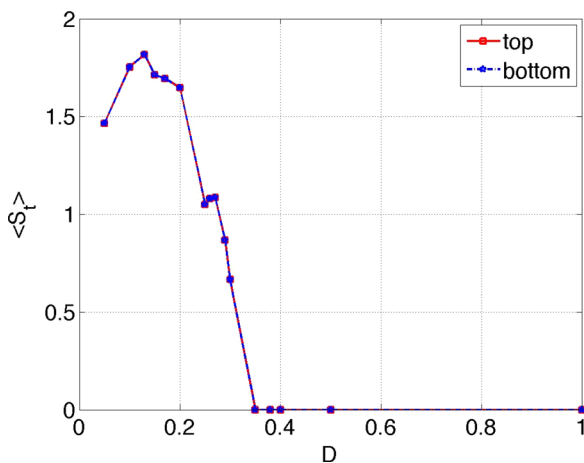


FIG. 5. Time-averaged spectral entropy for the pure diffusive instability.

Interactions among fingers characterized by succession of birth and death and the subsequent irregularity increase when D is decreased below D_c . This is coherent with the chaotic trend observed for large systems in the diffusively unstable regime.^{2,6,7}

This irregularity can be characterized thanks to the measure of the spectral entropy, defined as^{21–24}

$$S(t) = - \sum_{k=1}^N p_{k,t} \ln p_{k,t}, \quad (12)$$

where $p_{k,t}$ is the relative weight of mode k ,

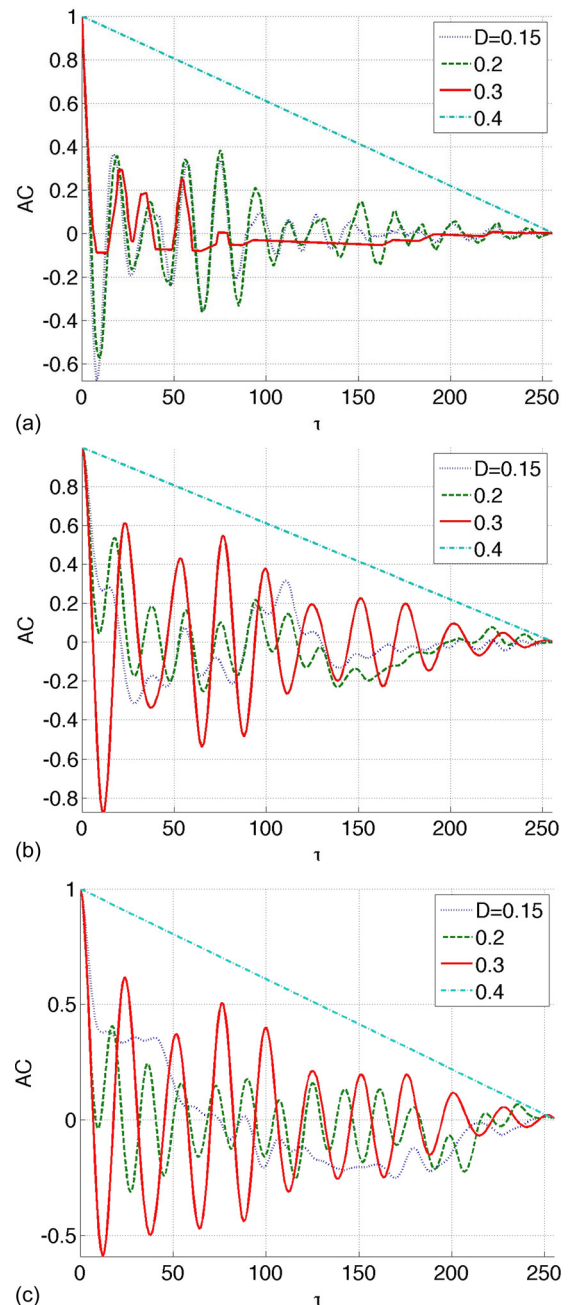


FIG. 6. Autocorrelation function AC as a function of the delay time τ for $D = 0.15-0.4$ at (a) $t = 1000$, (b) $t = 3000$, and (c) $t = 5000$.

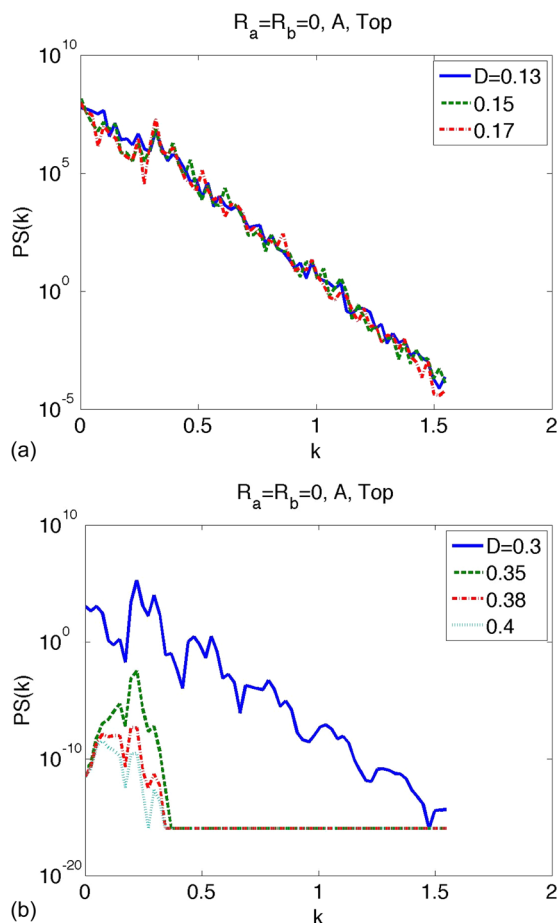


FIG. 7. Time-averaged power spectrum $PS(k)$ as a function of k for (a) $D = 0.13 - 0.17$ and (b) $D = 0.3 - 0.4$.

$$p_{k,t} = \frac{|c_{a,b}(k,t)|^2}{\sum_k |c_{a,b}(k,t)|^2} \tag{13}$$

Here, $\hat{c}_{a,b}$ is the discrete spatial Fourier transform of $c_{a,b}(y,t)$ given by

$$\hat{c}_{a,b}(k,t) = \sum_{j=0}^{N-1} c_{a,b}(j\Delta x,t) e^{-\sqrt{-1}j\Delta xk}, \tag{14}$$

where $k = 2\pi m/N$ and $m = 0, 1, 2, \dots, N$. This spectral entropy is a good measure of changes in the spatial patterns and in particular of the spatial disorder. If $p_{k,t} = 0$ we assume the product $p_{k,t} \ln p_{k,t} = 0$. Therefore, if $p_{k,t} = 1$ for some k , then $S(t) = 0$ (ordered state). The maximum entropy^{24,25} is $S(t) = \ln(N_y)$. For our system where $N_y = 256$, $S_{max}(t) \approx 5.5$.

To analyse the spectral entropy for each D , we calculated the time-averaged spectral entropy,²⁴ $\langle S \rangle_t$, corresponding to the mean of $S(t)$ in the time interval $0 \leq t \leq 5000$. In case of a transition to a complex dynamics, the spectral entropy suddenly increases. Hence, as long as $D > D_c$ where the front remains planar, the time-averaged spectral entropy $\langle S \rangle_t = 0$. However, once D is decreased below D_c , irregularity sets in and $\langle S \rangle_t$ departs from zero. This characteristic is shown in Figure 5. Interestingly, the largest spatial disorder is obtained when $D \approx 0.15$ ($\langle S \rangle_t \approx 1.9$).

If we analyse 15 different simulations with same values of parameters but different noise in the initial conditions, we obtain $\langle S \rangle_t = 2.20 \pm 0.12$ for $D = 0.15$ which we consider here as the representative value for the pure diffusive instability.

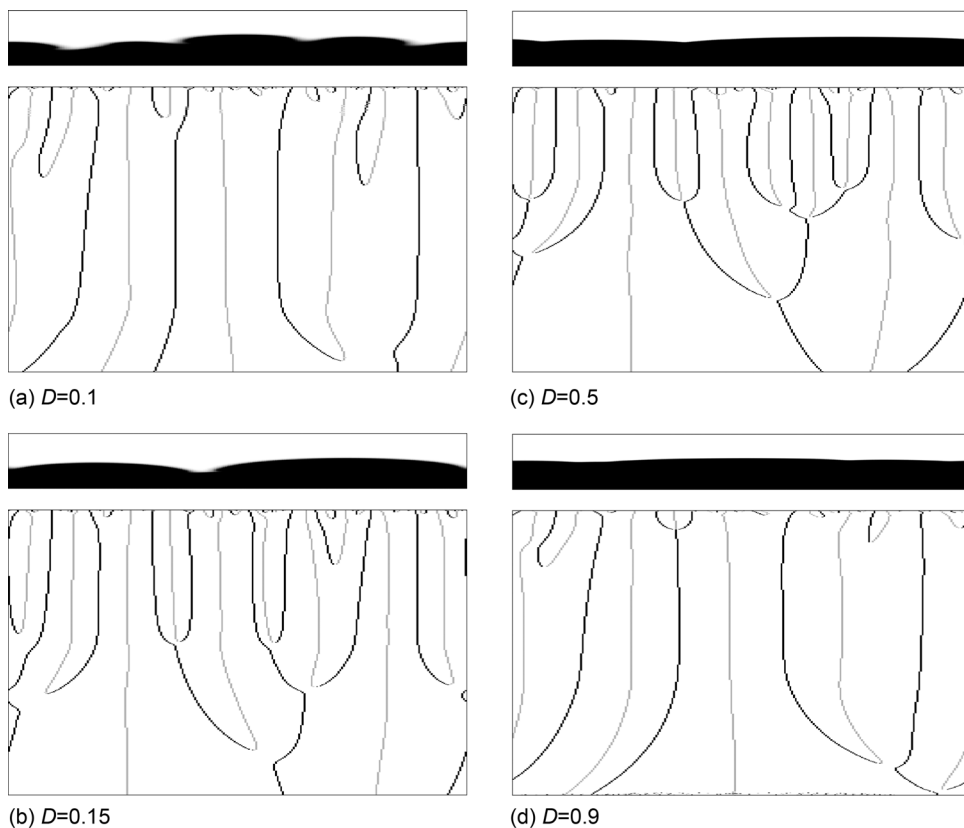


FIG. 8. Space-time map of the locations of the maxima (black) and minima (grey) of the longitudinally averaged profile of reactant A as a function of time for a buoyantly unstable ascending front for $R_a = 0.5, R_b = 0.25$, different values of D from $t = 0$ to $t = 5600$. On top, the concentration c_a at time $t = 5000$.

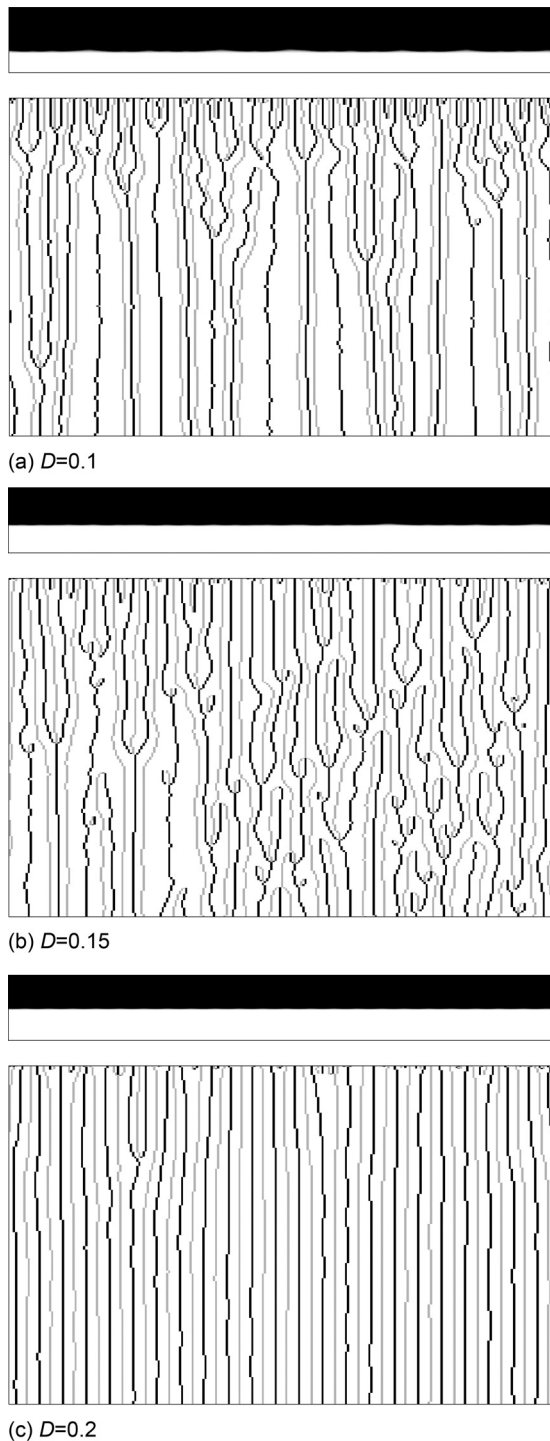


FIG. 9. Same as Fig. 8 but for a buoyantly stable descending front and $R_a > R_b$.

The front dynamics can also be characterized quantitatively by the autocorrelation function

$$C(t, \tau) = \frac{AC(\tau)}{AC(\tau = 0)}, \quad (15)$$

where

$$AC(\tau) = \frac{1}{N} \sum_{t=1}^{N-\tau} (c(t, y) - \bar{c}(t))(c(t + \tau, y) - \bar{c}(t)) \quad (16)$$

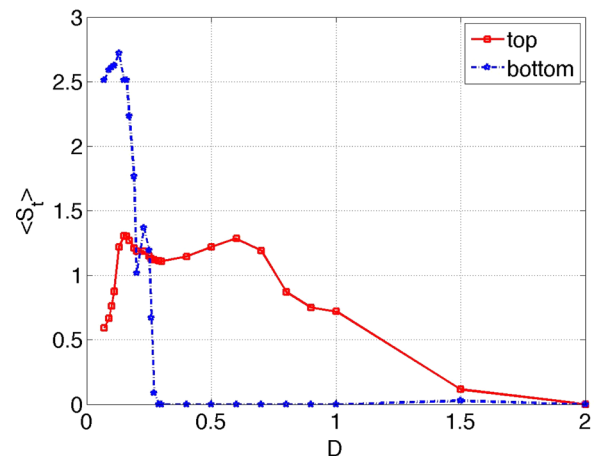


FIG. 10. Time-averaged spectral entropy for the system with $R_a > R_b$.

evaluated for each t . We chose three t at which to evaluate C : $t = 1000$, $t = 3000$, and $t = 5000$. Figure 6 shows the development of correlations in time.

The system with the largest spatial disorder ($D = 0.15$) presents some correlations at earlier time (see Fig. 6(a)) that do not persist later on (see Fig. 6(b)). However, for systems with $D > 0.15$, it is possible to observe a persistent short range correlation during the front evolution (see Figs. 6(b) and 6(c)). These short range correlations indicate a characteristic wavelength arising from the front instability, which can be analysed using the time-averaged power spectrum

$$PS(k) = \frac{1}{T} \sum_{t_i}^{t_f+T} \langle |\hat{c}_{a,b}|^2 \rangle. \quad (17)$$

This quantity is used to characterize the degree of spatial disorder. In Figure 7, the time-averaged power spectra show different degrees of spatial disorder for different values of the diffusion ratio. In each case, this quantity indicates similarities between the spatial patterns.

The largest degree of spatial disorder is observed for small values of D (see Fig. 7(a)). The results for the systems of Figure 6 are shown in Figure 7.

In this case, the time-averaged power spectrum shows a repetitive behaviour for $D = 0.3$ indicating the correlation observed in Figure 6. For $D = 0.15$, the time-averaged power spectrum indicates the growth of modes with smaller wave numbers. This dynamics corresponds to the appearance of structures on longer length scales which is in good agreement with predictions from the linear stability analysis.¹²

Let us now examine the results of such spectral analysis of the system when the influence of buoyancy effects is added, i.e., when the diffusive instability starts to interact with buoyancy-driven instabilities of the fronts ($R_{a,b} \neq 0$).

IV. BUOYANTLY UNSTABLE CHEMICAL FRONTS

The results of space-time maps of concentrations, correlation function and spectral analysis (spectral entropy and time averaged power spectra) when the RT and diffusive

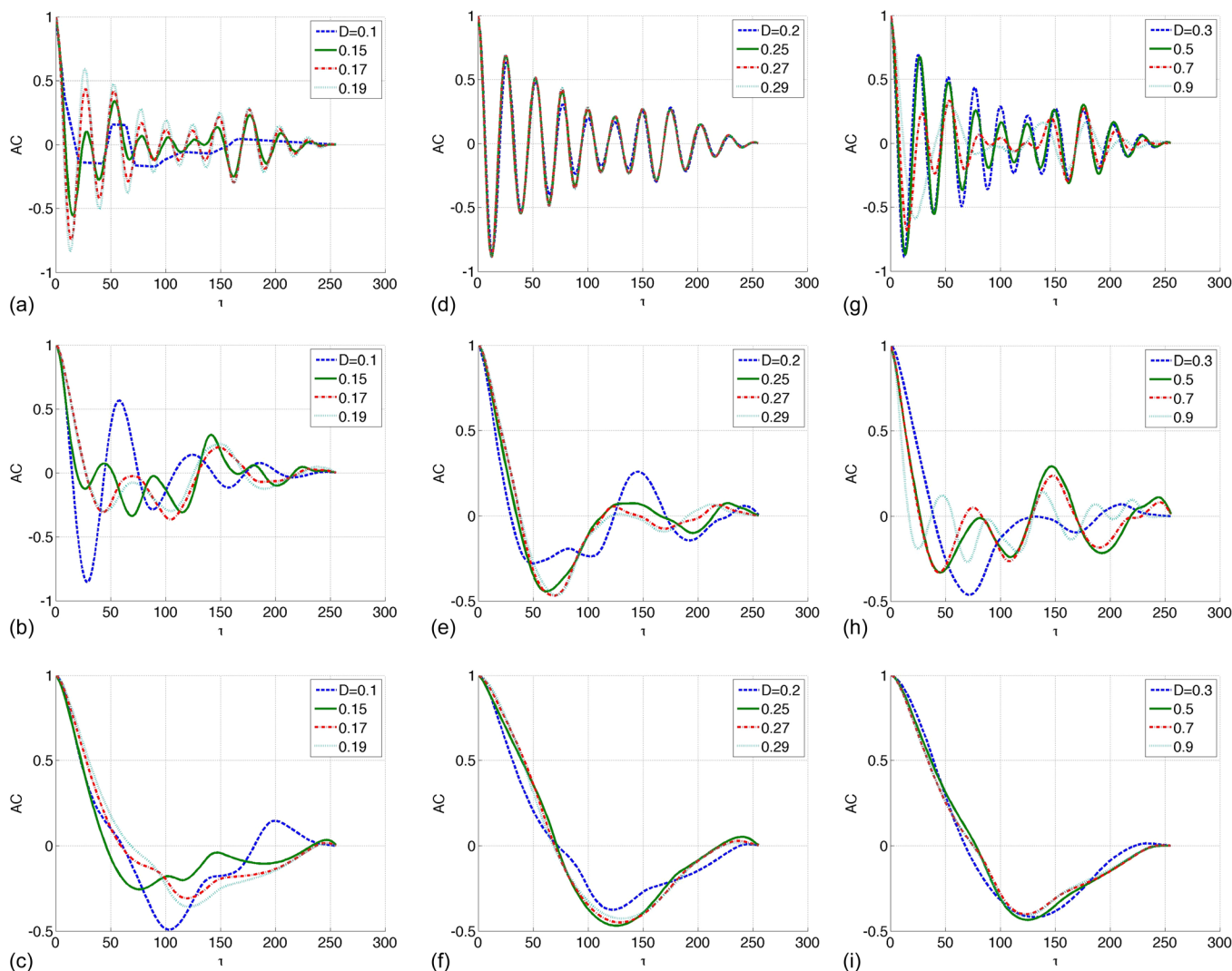


FIG. 11. Autocorrelation functions for the buoyantly unstable ascending front of reactant A (see Fig. 8) when $R_a > R_b$, at three times: $t = 1000$, $t = 3000$ and $t = 5000$.

instabilities interact are here analyzed when $R_a \neq R_b$ and $D < D_c$.

A. Case: $R_b = \alpha R_a$, $\alpha = 0.5$

In this case, the density decreases during the reaction as $R_b < R_a$, i.e., the solution of the product B is less dense than that of the reactant A . The ascending fronts are buoyantly unstable, while the descending fronts are convectively stable. Figures 8 and 9 illustrate the dynamics by space-time maps for ascending and descending fronts, respectively, when $R_a = 0.5$ and $R_b = 0.25$.

The space-time maps for the ascending fronts (Fig. 8) show a small wavelength in the beginning of the simulation. The merging of lines observed during the time evolution indicates coalescence of fingers towards one single finger²⁰ occurring faster for $D > D_c$. Here, the RT instability is acting and a pattern with a larger wavelength is, therefore, still present when $D > D_c$. For buoyantly stable descending fronts (Fig. 9), the defects observed in spatio-temporal maps decrease as D increases (Figs. 9(a)–9(c)) and the system tends to a planar state for $D > D_c$, i.e., no modulation is seen

on space-time maps. For small D , the diffusive instability dominates and a great number of fingers with a smaller wavelength are observed. As the system evolves, they coalesce and divide due to buoyancy forces. However, as a comparison with Figure 4 shows, the irregularity is different in the presence of density changes (Fig. 9) then when the diffusive instability is the only one to be operative (Fig. 4).

The degree of irregularity of spatial patterns can be quantified by the time-averaged spectral entropy (see Fig. 10). For descending fronts, the spectral entropy reaches the largest value $\langle S \rangle_t \approx 2.7$ when D is small and then decreases quickly. An ordered state is reached when $D > 0.25$. For ascending fronts, RT takes over for larger D and the value of spatial disorder remains $\langle S \rangle_t \approx 1.2$ up to $D \approx 0.7$ and then decreases indicating a transition to an ordered state. This result agrees with the linear stability analysis, which shows larger growth rates of disturbances for small D and ascending fronts.³

In order to establish the entropy for systems where either the RT instability or diffusive instability dominates, fifteen different simulations are evaluated for the system with the largest entropy value in Figure 10: $D = 0.1$. The average

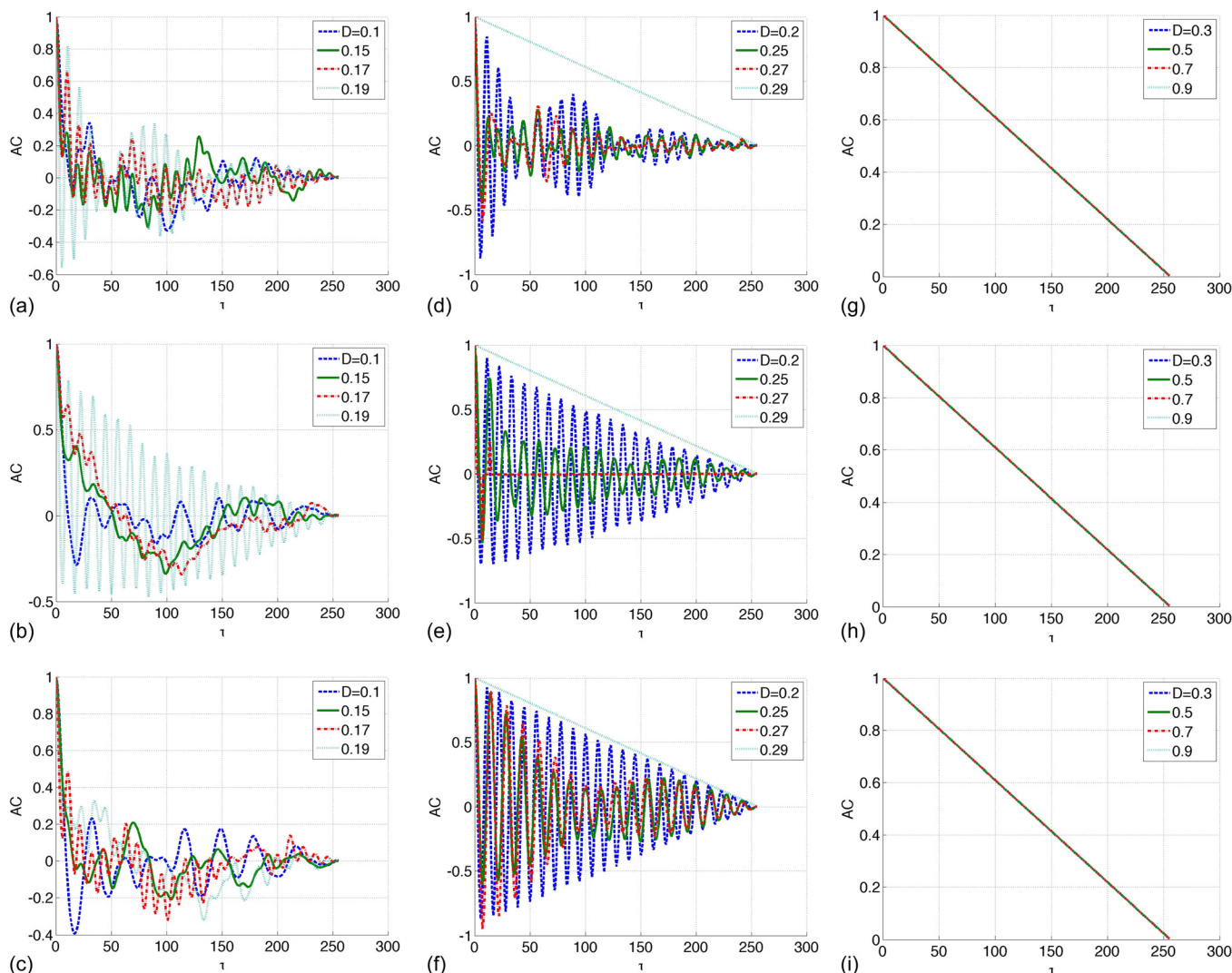


FIG. 12. Autocorrelation functions for the buoyantly stable descending front of reactant A as seen on Fig. 9 when $R_a > R_b$ at three times: $t = 1000$, $t = 3000$ and $t = 5000$.

value of the spectral entropy for the ascending fronts is $\langle S \rangle_t = 0.89 \pm 0.09$, and for the descending fronts is $\langle S \rangle_t = 2.38 \pm 0.07$. We can conclude, by comparing the results from spectral entropy and space-time maps, that the first value represents the value of entropy for a system dominated by the RT instability, while the second value corresponds to a system dominated by the diffusive instability with $R_a > R_b$. This last value is slightly larger than $\langle S \rangle_t = 2.20$ computed for the diffusive instability case with $R_a = R_b = 0$.

The dynamics of the autocorrelation function for results of Figs. 8 and 9 is shown in Figs. 11 and 12 at three different times. For $t = 1000$, we analyze the behavior of the system close to onset of its evolution. At $t = 3000$ and 5000, we address the properties of the system in the middle and final stages of its evolution, respectively. Also, each set of data corresponds to a value of D allowing us to compare different systems.

The first data set (Figures 11(a)–11(c)) focuses on D in the range $[0.1–0.2]$. Differences between the autocorrelation functions, especially the curve corresponding to $D = 0.1$ stand out at $t = 3000$ (see Fig. 11(b)). Compared with the

space-time map, at this point in the evolution, the RT instability dominates the structure formation. At $t = 5000$, i.e., the end of the simulation, the autocorrelation function does not show indication of periodicity any longer, but some persistent oscillations are still present. Looking at the space-time maps, the propagation front is almost stable with some RT fingers remaining.

The second data set for D from 0.2 to 0.3 shows that the correlations are almost identical at the beginning of the simulations (Figure 11(d)), have decreased when $t = 3000$ (Figure 11(e)) and vanish at $t = 5000$ (Figure 11(f)). For $0.3 < D < 1$ (third data set), and as expected from the linear stability analysis, some periodicity is noticed in the beginning of the simulations (Figure 11(g)) but when fingers from the RT instability dominate ($D \sim 0.9$), a periodic behavior in the autocorrelation function may be seen at $t = 3000$ (Figure 11(h)). It vanishes when $t = 5000$ (Figure 11(i)).

For descending fronts, the same procedure is applied and gives the autocorrelation functions of Fig. 12. In the first data for $0.1 < D < 0.2$, a transient periodic behavior is observed when $D = 0.19$ (Figs. 12(a)–12(c)). When t

approaches 5000, however, such a function is no longer periodic (Fig. 12(c)). In the second data for D from 0.2 to 0.3 (Figs. 12(d)–12(f)), we see that the periodicity for $D = 0.2$ increases in time. This is the signature of the regular small wavelength pattern of the diffusive instability. Compared with the space-time maps, this behavior is similar to that observed for $R_a = R_b = 0$ and $D = 0.3$. Thus, the autocorrelation function has a shorter wavelength. However, in this data set, we observe that there is no correlation for $D = 0.29$. This result was expected from the analysis of spectral entropy, which indicates the tendency of the system to evolve to a homogeneous state for $D > 0.3$ which is confirmed in the third set of data where no correlation can be noted (Figs. 12(g)–12(i)).

Comparison of the time-averaged power spectra show that, for the buoyantly unstable ascending front, the degree of spatial disorder is largest for small values of D , when small undulations are observed in Fourier modes (Fig. 13(a)). These undulations disappear as D increases (Fig. 13(b)).

For buoyantly stable descending fronts, systems that showed some periodicity in the autocorrelation function present in the time-averaged power spectra similar behavior, in particular systems with $D = 0.19$ (Fig. 14(a)) and $D = 0.2$ (Fig. 14(b)). For systems with $0.2 < D < 0.3$, we can set the period off for each case (Fig. 14(b)). Moreover, the peaks are nearly coincident, with respect to the Fourier mode, indicating that there was a scattering of spectral

energy to other modes as D decreases. As expected, as D increases, no period can be observed in the power spectrum (see Fig. 14(c)).

B. Case: $R_b = \alpha R_a$, $\alpha = 2$

In this case, the density increases during the reaction as the product B is denser than the reactant A. The ascending fronts are hence buoyantly stable, while the descending fronts are unstable. Figure 15 shows the dynamics for descending fronts. The system is here both buoyantly and diffusively unstable if $D < D_c$ which is known to produce spatiotemporal chaos. The complex dynamics in space-time maps shows indeed an irregular succession of merging and splitting of fingers indicating the interplay between RT and

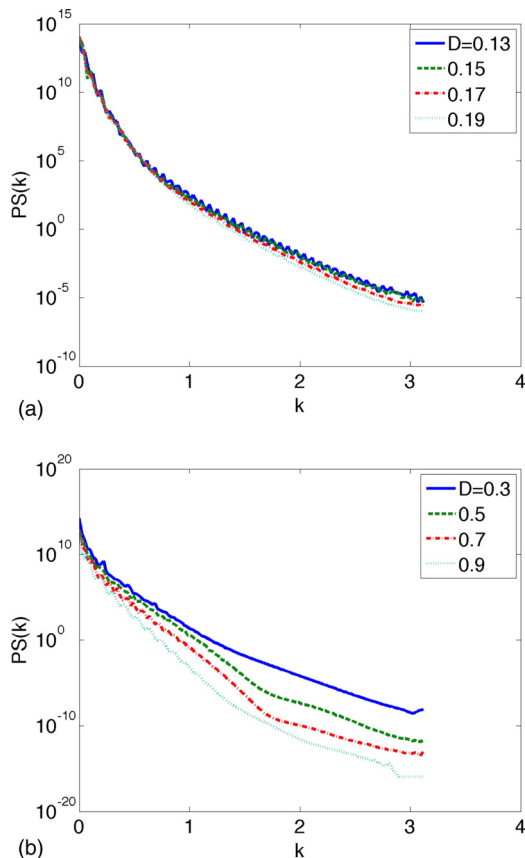


FIG. 13. Time-averaged power spectra for the reactant A in the buoyantly unstable ascending fronts for $R_a > R_b$ and different values of D .

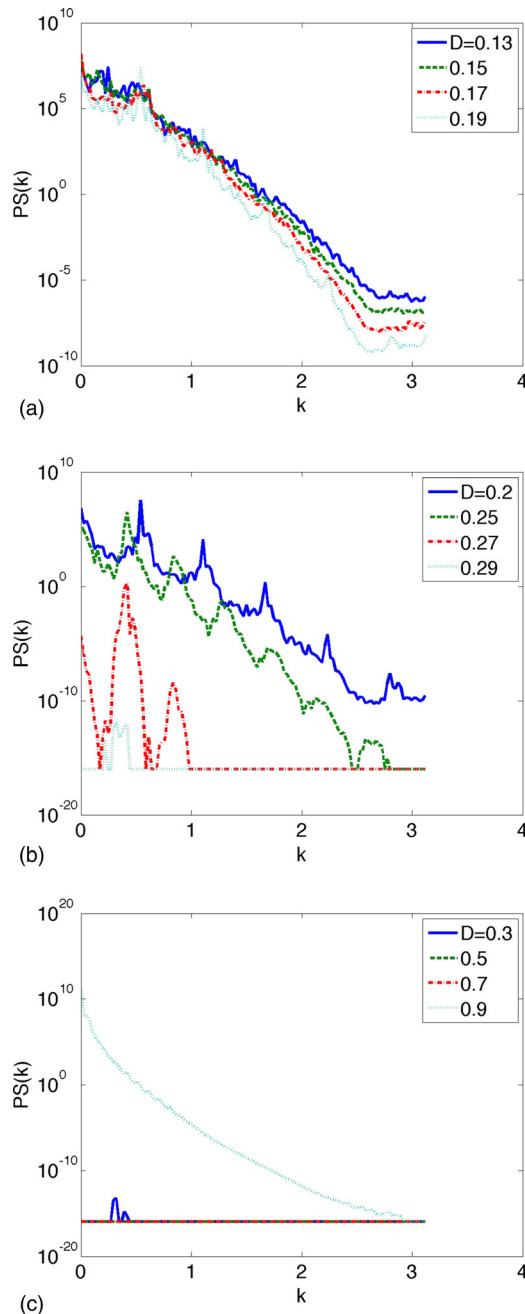


FIG. 14. Same as in Fig. 13 but for buoyantly stable descending fronts.

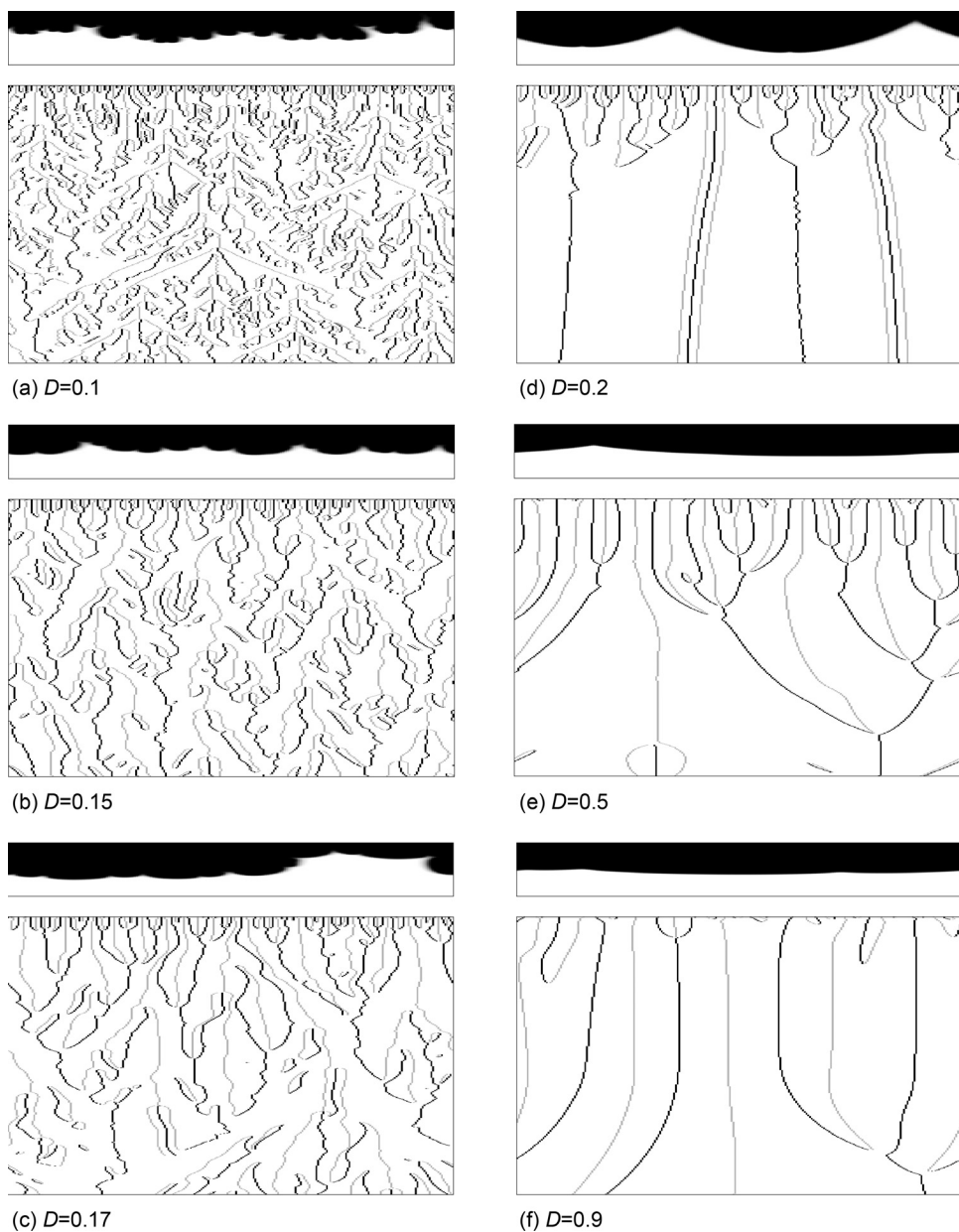


FIG. 15. Space-time map of the locations of the maxima (black) and minima (grey) of the longitudinally averaged profile of reactant A as a function of time when the density increases during the reaction for different values of D for buoyantly unstable descending fronts from $t=0$ to $t=5600$. On top, the concentration of reactant A is shown at time $t=5000$.

diffusive instabilities. When D increases above D_c , large fingers due to the pure RT instability are the only ones remaining.⁴

The time-averaged spectral entropy reaches the largest values when RT and diffusive instabilities interact, i.e., for descending fronts (bottom) when $D < D_c$ (Fig. 16). This quantity suddenly decays indicating a transition to an intermediate value of spatial disorder. This value almost does not change ($\langle S \rangle_t \approx 1, 1$) up to $D \cong 0.7$. The large fingers due to a Rayleigh-Taylor instability are predominant for larger D . The tendency to a more homogeneous state occurs when $\langle S \rangle_t$ decreases when $D > 1$, as predicted by linear stability analysis.⁵

For ascending fronts, the stabilizing buoyancy effects kill the unstable diffusive modes and $\langle S \rangle_t$ remains zero. Figure 17 shows the autocorrelation function for various values of D when the RT instability interacts with the diffusive instability. For $0.1 < D < 0.2$, the autocorrelation function has no periodicity and the curve oscillates unpredictably

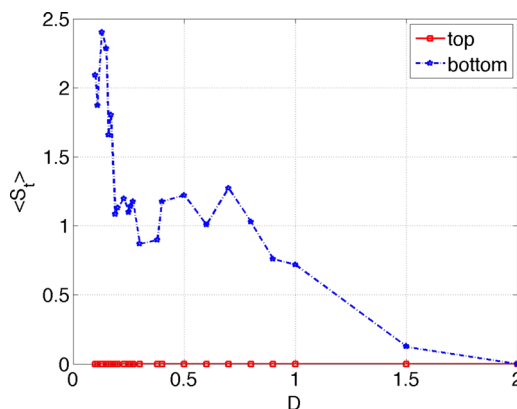


FIG. 16. Time-averaged spectral entropy for the system with $R_a < R_b$ for descending fronts unstable both from RT and diffusive instabilities.

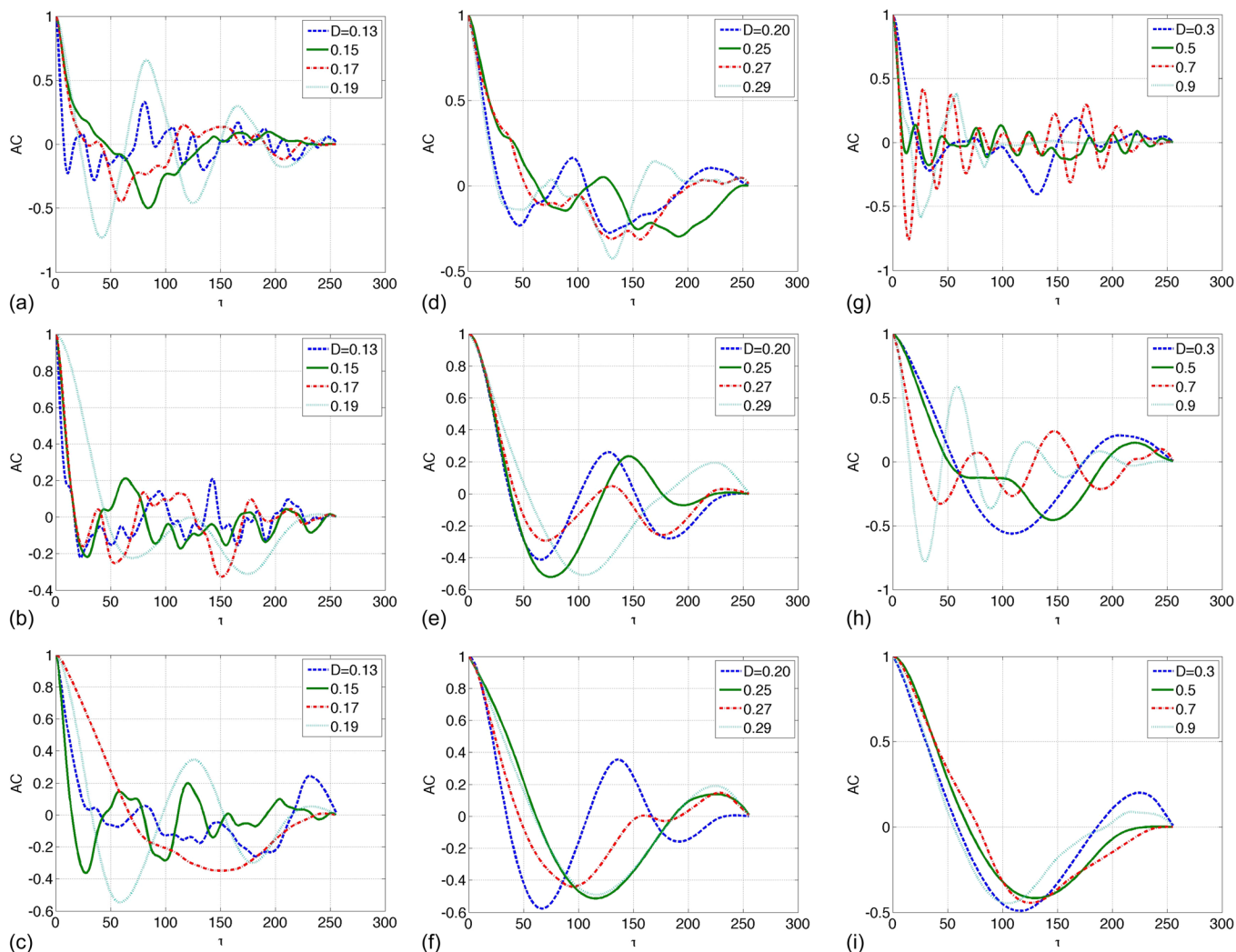


FIG. 17. Autocorrelation function C of the descending front for the reactant A when $R_b > R_a$ at three points in time: $t = 1000$, $t = 3000$, and $t = 5000$.

around zero (see Figs. 17(a)–17(c)). For $D = 0.19$, we can notice a characteristic wavelength, larger than that observed when $D = 0.2$ in Figure 12. It indicates the presence of structures with larger size due to RT modes. A similar situation is present when $0.2 < D < 0.3$. After a transient situation for $t \lesssim 1000$, the autocorrelation function exhibits a typical behavior in the presence of large structures (see Figs. 17(d)–17(f)).

For the last data set, we study cases where the spectral entropy shows an intermediate value of spatial disorder. The corresponding space-time maps indicate the prevalence of the RT instability. Note that some periodicity can be observed up to half of the simulation evolution (see Figs. 17(g)–17(i)). At the end of the simulations, the autocorrelation function exhibits a behavior similar to that of systems with a single finger (see Fig. 17(i)).

The time-averaged power spectra show a similarity among the spatial patterns obtained for $D < 0.1$ (Figure 18(a)) and $0.2 < D < 0.3$ (Figure 18(b)). The small oscillations present in the curves of the time-averaged power spectra indicate the presence of disturbances in the system, caused by the diffusive instability, which spreads the spectral energy in Fourier mode.

V. CONCLUDING REMARKS

We have shown that spectral analysis using longitudinally averaged profiles is a useful methodology to study the dynamics of unstable chemical fronts. By means of time-averaged spectral entropy and analysis of autocorrelation functions, it is possible to characterize the complex dynamics of buoyantly and diffusively unstable propagating fronts. Spectral entropy identifies and quantifies the transition to spatio-temporal chaos when both RT and diffusive instabilities interact. From the autocorrelation function, we are able to find either the wavelength of the front modulation or to identify possible chaotic behavior. Also, the time-averaged power spectra can be used to verify such results.

Figures 19(a) and 19(b) summarize the results for the spectral entropy of ascending and descending fronts respectively. For the ascending front (Fig. 19) and $D > D_c$, the RT instability dominates if $R_a > R_b$ and the corresponding $\langle S \rangle_t$ is then positive in a larger domain of D than for $R_a = R_b = 0$ where $\langle S \rangle_t \neq 0$ only in the diffusively unstable regime. This result indicates that the disorder due to the RT instability is not so high compared with the spatio-temporal chaos in the form of biscale chaos⁷ caused by diffusive instability.

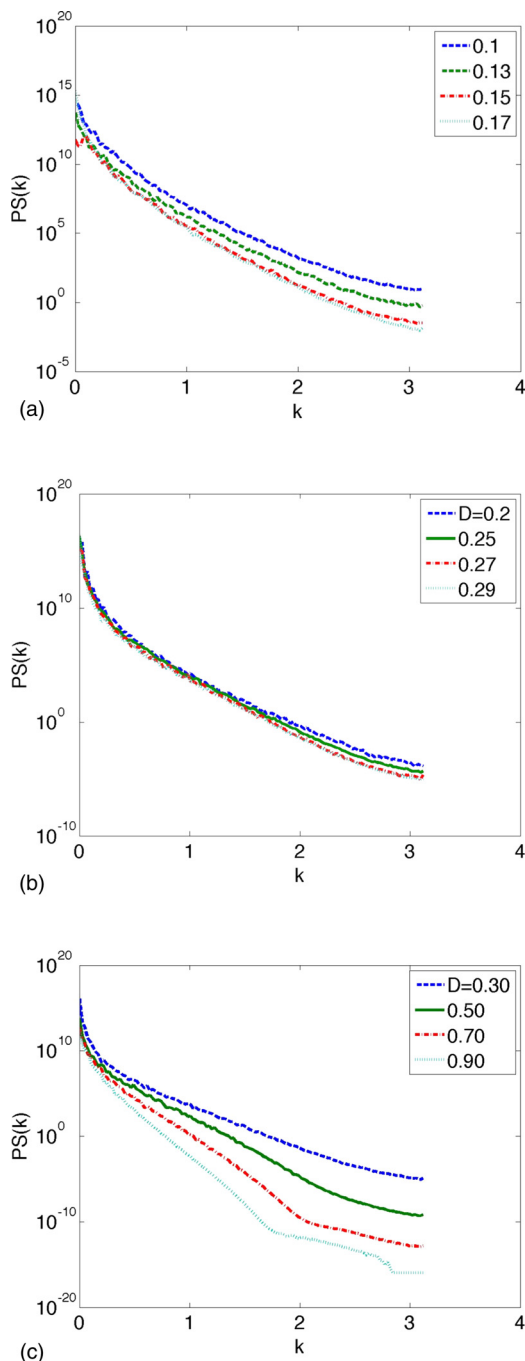


FIG. 18. Time-averaged power spectra for the descending fronts of the reactant A to the system $R_a < R_b$ and different values of D .

Therefore, it is clear that the diffusive instability provides patterns with a larger degree of spatial disorder, and a transition to more complex dynamics. Furthermore, it indicates that the RT instability leads to structures with more regular periodic dynamics. If $R_b > R_a$, the density stratification is stabilizing and kills the diffusive instability. As a consequence, $\langle S \rangle_t = 0$, even for $D < D_c$.

In the case of descending fronts (Fig. 19(b)), if $R_a > R_b$, the system is buoyantly stable and the only disorder comes from the diffusive instability when $D < D_c$. The time-averaged power spectrum indicates that the system has some periodicity before becoming ordered (low spatial disorder). In other words, the dynamics changes from a complex

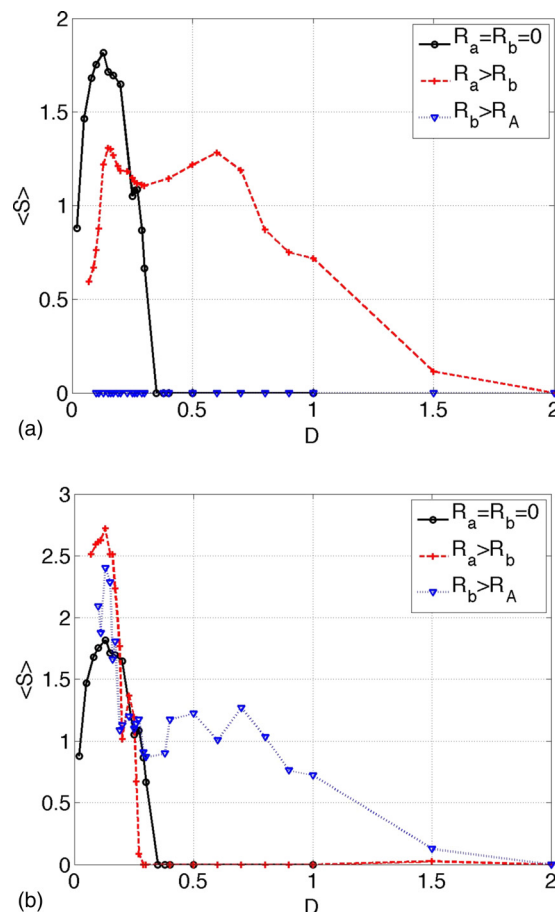


FIG. 19. Comparison of spectral entropy for (a) ascending fronts and (b) descending fronts.

pattern to a periodic one. When $R_b > R_a$, the interaction between the RT and diffusive instabilities leads to a very complex dynamics (Fig. 15) characterized by the largest value of $\langle S \rangle_t$ (Fig. 19(b)). However, if the diffusion rate D increases, this interaction decreases and the RT instability takes over. The intensity of spatial disorder decreases then to an intermediate value, while space-time maps show a switch to one single dominant finger.

In conclusion, this work has quantified the degree of complexity of spatiotemporal patterns obtained when diffusive and RT instabilities act on traveling fronts to yield spatiotemporal chaos. We have developed several quantitative measurements which could easily be applied on experimental data to gain more insight into new STC dynamics resulting from the interplay between two different instabilities.

ACKNOWLEDGMENTS

The authors acknowledge financial support from UFABC, CNPq, ULB, FNRS and the Communauté Française de Belgique (ARC programme). The authors thank J. D’Heroncourt, D. Horváth, A. Tóth, E. L. Rempel, R. R. Rosa, P. Gaspard, H. L. Swinney, and J. Merkin for fruitful discussions.

¹A. De Wit, G. Dewel, and P. Borckmans, *Phys. Rev. E* **48**, R4191 (1993).
²J. D’Heroncourt, J. H. Merkin, and A. De Wit, *Phys. Rev. E* **76**, 035301R (2007).

- ³J. D'Heroncourt, J. H. Merkin, and A. De Wit, *J. Chem. Phys.* **130**, 114502 (2009).
- ⁴J. D'Heroncourt, J. H. Merkin, and A. De Wit, *J. Chem. Phys.* **130**, 114503 (2009).
- ⁵T. Rica, E. Pópity-Tóth, D. Horváth, and A. Tóth, *Physica D* **239**, 831 (2010).
- ⁶D. Horváth, V. Petrov, S. K. Scott, and K. Showalter, *J. Chem. Phys.* **98**, 6332 (1993).
- ⁷A. Malevanets, A. Careta, and R. Kapral, *Phys. Rev. E* **52**, 4724 (1995).
- ⁸D. Horváth and K. Showalter, *J. Chem. Phys.* **102**, 2471 (1995).
- ⁹A. Tóth, I. Lagzi, and D. Horváth, *J. Phys. Chem.* **100**, 14837 (1996).
- ¹⁰D. Horváth and A. Tóth, *J. Chem. Phys.* **108**, 1447 (1998).
- ¹¹M. Fuentes, M. N. Kuperman, and P. De Kepper, *J. Phys. Chem. A* **105**, 6769 (2001).
- ¹²J. H. Merkin and I. Z. Kiss, *Phys. Rev. E* **72**, 026219 (2005).
- ¹³A. De Wit, *Phys. Rev. Lett.* **87**, 054502 (2001).
- ¹⁴I. R. Epstein and J. A. Pojman, *An Introduction to Nonlinear Chemical Dynamics* (Oxford University Press, 1998).
- ¹⁵J. D'Heroncourt, A. Zebib, and A. De Wit, *Chaos* **17**, 013109 (2007).
- ¹⁶M. Böckmann and S. C. Müller, *Phys. Rev. Lett.* **85**, 2506 (2000).
- ¹⁷D. Horváth, T. Bánsági, Jr., and A. Tóth, *J. Chem. Phys.* **117**, 4399 (2002).
- ¹⁸C. T. Tan and G. M. Homsy, *Phys. Fluids* **31**, 1330 (1988).
- ¹⁹W. B. Zimmerman and G. M. Homsy, *Phys. Fluids A* **3**, 1859 (1991).
- ²⁰A. De Wit, *Phys. Fluids* **16**, 163 (2004).
- ²¹G. E. Powell and I. C. Percival, *J. Phys. A* **12**, 2053 (1979).
- ²²H. Xi and J. D. Gunton, *Phys. Rev. E* **52**, 4963 (1995).
- ²³R. V. Cakmur, D. A. Egolf, B. B. Plapp, and E. Bodenschatz, *Phys. Rev. Lett.* **79**, 1853 (1997).
- ²⁴E. L. Rempel, A. C.-L. Chian, and R. A. Miranda, *Phys. Rev. E* **76**, 056217 (2007).
- ²⁵R. Badii and A. Politi, *Complexity: Hierarchical Structures and Scaling in Physics* (Cambridge University Press, 1997).